

Sliced Wasserstein Distance for Learning Gaussian Mixture Models

Soheil Kolouri
HRL Laboratories, LLC
skolouri@hrl.com

Gustavo K. Rohde
University of Virginia
gustavo@virginia.edu

Heiko Hoffmann
HRL Laboratories, LLC
hhoffmann@hrl.com

Abstract

Gaussian mixture models (GMM) are powerful parametric tools with many applications in machine learning and computer vision. Expectation maximization (EM) is the most popular algorithm for estimating the GMM parameters. However, EM guarantees only convergence to a stationary point of the log-likelihood function, which could be arbitrarily worse than the optimal solution. Inspired by the relationship between the negative log-likelihood function and the Kullback-Leibler (KL) divergence, we propose an alternative formulation for estimating the GMM parameters using the sliced Wasserstein distance, which gives rise to a new algorithm. Specifically, we propose minimizing the sliced-Wasserstein distance between the mixture model and the data distribution with respect to the GMM parameters. In contrast to the KL-divergence, the energy landscape for the sliced-Wasserstein distance is more well-behaved and therefore more suitable for a stochastic gradient descent scheme to obtain the optimal GMM parameters. We show that our formulation results in parameter estimates that are more robust to random initializations and demonstrate that it can estimate high-dimensional data distributions more faithfully than the EM algorithm.

1. Introduction

Finite Gaussian Mixture Models (GMMs), also called Mixture of Gaussians (MoG), are powerful, parametric, and probabilistic tools that are widely used as flexible models for multivariate density estimation in various applications concerning machine learning, computer vision, and signal/image analysis. GMMs have been utilized for: image representation [5, 17] to generate feature signatures, point set registration [24], adaptive contrast enhancement [9], inverse problems including super-resolution and deblurring [19, 55], time series classification [8], texture segmentation [43], and robotic visuomotor transformations [23] among many others.

As a special case of general latent variable models, finite GMM parameters could serve as a concise embedding [40], which provide a compressed representation of the data.

Moreover, GMMs could be used to approximate any density defined on \mathbb{R}^d with a large enough number of mixture components. To fit a finite GMM to the observed data, one is required to answer the following questions: 1) how to estimate the number of mixture components needed to represent the data, and 2) how to estimate the parameters of the mixture components. Several techniques have been introduced to provide an answer for the first question [37]. The focus of this paper is on the latter question.

The existing methods to estimate the GMM parameters are based on minimizing the negative log-likelihood (NLL) of the data with respect to the parameters [51]. The Expectation Maximization (EM) algorithm [15] is the prominent way of minimizing the NLL (though, see, e.g., as an alternative [38, 22]). While EM remains the most popular method for estimating GMMs, it only guarantees convergence to a stationary point of the likelihood function. On the other hand, various studies have shown that the likelihood function has bad local maxima that can have arbitrarily worse log-likelihood values compared to any of the global maxima [22, 25, 2]. More importantly, Jin et al. [24] proved that with random initialization, the EM algorithm will converge to a bad critical point with high probability. This issue turns the EM algorithm sensitive to the choice of initial parameters.

In the limit (i.e. having infinite i.i.d samples), minimizing the NLL function is equivalent to minimizing the Kullback-Leibler divergence between the data distribution and the GMM, with respect to the GMM parameters. Here, we propose, alternatively, to minimize the p-Wasserstein distance, and more specifically the sliced p-Wasserstein distance [28], between the data distribution and the GMM. The Wasserstein distance and its variations have attracted a lot of attention from the Machine Learning (ML) and signal processing communities lately [28, 3, 16]. It has been shown that optimizing with respect to the Wasserstein loss has various practical benefits over the KL-divergence loss [44, 16, 39, 3, 20]. Importantly, unlike the KL-divergence and its related dissimilarity measures (e.g. Jensen-Shannon divergence), the Wasserstein distance can provide a meaningful notion of closeness (i.e. distance) for distributions supported on non-overlapping low dimensional manifolds. This motivates our proposed

formulation for estimating GMMs.

To overcome the computational burden of the Wasserstein minimization for high-dimensional distributions, we propose to use the sliced Wasserstein distance [6, 30, 28]. Our method slices the high-dimensional data distribution via random projections and minimizes the Wasserstein distance between the projected one-dimensional distributions with respect to the GMM parameters. We note that the idea of characterizing a high-dimensional distribution via its random projections has been studied in various work before [52, 26]. The work in [26], for instance, minimizes the L_1 norm between the slices of the data distribution and the GMM with respect to the parameters. This method, however, suffers from the same shortcomings as the KL-divergence based methods.

The p-Wasserstein distances and more generally the optimal mass transportation problem have recently gained plenty of attention from the computer vision and machine learning communities [28, 49, 42, 29, 54, 47, 3]. We note that the p-Wasserstein distances have also been used in regard to GMMs, however, as a distance metric to compare various GMM models [11, 34, 45]. Our proposed method, on the other hand, is an alternative framework for fitting a GMM to data via sliced p-Wasserstein distances.

In what follows, we first formulate the p-Wasserstein distance, the Radon transform, and the Sliced p-Wasserstein distance in Section 2. In Section 3, we reiterate the connection between the K-means problem and the Wasserstein means problem [21], extend it to GMMs, and formulate the Sliced Wasserstein means problem. Our numerical experiments are presented in Section 4. Finally, we conclude our paper in Section 5.

2. Preliminary

2.1. p-Wasserstein distance:

In this section we review the preliminary concepts and formulations needed to develop our framework. Let $P_p(\Omega)$ be the set of Borel probability measures with finite p 'th moment defined on a given metric space (Ω, d) , and let $\rho \in P_p(X)$ and $\nu \in P_p(Y)$ be probability measures defined on $X, Y \subseteq \Omega$ with corresponding probability density functions I_x and I_y , $d\rho(x) = I_x(x)dx$ and $d\nu(y) = I_y(y)dy$. The p-Wasserstein distance for $p \in [1, \infty)$ between ρ and ν is defined as the optimal mass transportation (OMT) problem [53] with cost function $c(x, y) = d^p(x, y)$, such that:

$$W_p(\rho, \nu) = \left(\inf_{\gamma \in \Gamma(\rho, \nu)} \int_{X \times Y} d^p(x, y) d\gamma(x, y) \right)^{\frac{1}{p}}, \quad (1)$$

where $\Gamma(\rho, \nu)$ is the set of all transportation plans, $\gamma \in \Gamma(\rho, \nu)$, and satisfy the following:

$$\begin{aligned} \gamma(A \times Y) &= \rho(A) & \text{for any Borel subset } A \subseteq X \\ \gamma(X \times B) &= \nu(B) & \text{for any Borel subset } B \subseteq Y \end{aligned} .$$

Due to Brenier's theorem [7], for absolutely continuous probability measures ρ and ν (with respect to Lebesgue measure) the p-Wasserstein distance can be equivalently obtained from,

$$W_p(\rho, \nu) = \left(\inf_{f \in MP(\rho, \nu)} \int_X d^p(f(x), x) d\rho(x) \right)^{\frac{1}{p}} \quad (2)$$

where, $MP(\rho, \nu) = \{f : X \rightarrow Y \mid f_{\#}\rho = \nu\}$ and $f_{\#}\rho$ represents the pushforward of measure ρ ,

$$\int_{f^{-1}(A)} d\rho(x) = \int_A d\nu(y) \text{ for any Borel subset } A \subseteq Y.$$

When a transport map exists, the transport plan and the transport map are related via, $\gamma = (\text{Id} \times f)_{\#}\rho$. Note that in most engineering and computer science applications Ω is a compact subset of \mathbb{R}^d and $d(x, y) = |x - y|$ is the Euclidean distance. By abuse of notation we will use $W_p(\rho, \nu)$ and $W_p(I_x, I_y)$ interchangeably throughout the manuscript. For a more detailed explanation of the Wasserstein distances and the optimal mass transport problem, we refer the reader to the recent review article by Kolouri et al. [28] and the references there in.

One-dimensional distributions: The case of one-dimensional continuous probability measures is specifically interesting as the p-Wasserstein distance has a closed form solution. More precisely, for one-dimensional probability measures there exists a unique monotonically increasing transport map that pushes one measure into another. Let $J_x(x) = \rho((-\infty, x]) = \int_{-\infty}^x I_x(\tau) d\tau$ be the cumulative distribution function (CDF) for I_x and define J_y to be the CDF of I_y . The transport map is then uniquely defined as, $f(x) = J_y^{-1}(J_x(x))$ and consequently the p-Wasserstein distance is calculated as:

$$\begin{aligned} W_p(\rho, \nu) &= \left(\int_X d^p(J_y^{-1}(J_x(x)), x) d\rho(x) \right)^{\frac{1}{p}} \\ &= \left(\int_0^1 d^p(J_y^{-1}(z), J_x^{-1}(z)) dz \right)^{\frac{1}{p}} \end{aligned} \quad (3)$$

where in the second line we used the change of variable $J_x(x) = z$. The closed form solution of the p-Wasserstein is an attractive property that gives rise to the Sliced-Wasserstein (SW) distances. Next we review the Radon transform, which enables the definition the Sliced p-Wasserstein distance.

2.2. Radon transform

The d -dimensional Radon transform, \mathcal{R} , maps a function $I \in L^1(\mathbb{R}^d)$ where $L^1(\mathbb{R}^d) := \{I : \mathbb{R}^d \rightarrow \mathbb{R} \mid \int_{\mathbb{R}^d} |I(x)| dx \leq \infty\}$ to the set of its integrals over the hyperplanes of \mathbb{R}^d and is defined as,

$$\mathcal{R}I(t, \theta) := \int_{\mathbb{R}^d} I(x) \delta(t - x \cdot \theta) dx \quad (4)$$

For all $\theta \in \mathbb{S}^{d-1}$ where \mathbb{S}^{d-1} is the unit sphere in \mathbb{R}^d . Note that $\mathcal{R} : L^1(\mathbb{R}^d) \rightarrow L^1(\mathbb{R} \times \mathbb{S}^{d-1})$. For the sake of completeness, we note that the Radon transform is an invertible, linear transform and we denote its inverse as \mathcal{R}^{-1} , which is also known as the filtered back projection algorithm and is defined as:

$$\begin{aligned} I(x) &= \mathcal{R}^{-1}(\mathcal{R}I(t, \theta)) \\ &= \int_{\mathbb{S}^{d-1}} (\mathcal{R}I(\cdot, \theta) * h(\cdot)) \circ (x \cdot \theta) d\theta \end{aligned} \quad (5)$$

where $h(\cdot)$ is a one-dimensional filter with corresponding Fourier transform $\mathcal{F}h(\omega) = c|\omega|^{d-1}$ (it appears due to the Fourier slice theorem, see [41] for more details) and ‘*’ denotes convolution. Radon transform and its inverse are extensively used in Computerized Axial Tomography (CAT) scans in the field of medical imaging, where X-ray measurements integrate the tissue-absorption levels along 2D hyper-planes to provide a tomographic image of the internal organs. Note that in practice acquiring infinite number of projections is not feasible therefore the integration in Equation (5) is replaced with a finite summation over projection angles. A formal measure theoretic definition of Radon transform for probability measures could be found in [6].

Radon transform of empirical PDFs: The Radon transform of I_x simply follows Equation (4). However, in most machine learning applications we do not have access to the distribution I_x but to its samples, x_n . Kernel density estimation could be used in such scenarios to approximate I_x from its samples,

$$I_x(x) \approx \frac{1}{N_\rho} \sum_{n=1}^{N_\rho} \phi(x - x_n)$$

where $\phi : \mathbb{R}^d \rightarrow \mathbb{R}^+$ is a density kernel where $\int_{\mathbb{R}^d} \phi(x) dx = 1$ (e.g. Gaussian kernel). The Radon transform of I_x can then be approximated from its samples via:

$$\mathcal{R}I_x(t, \theta) \approx \frac{1}{N_\rho} \sum_{n=1}^{N_\rho} \mathcal{R}\phi(t - x_n \cdot \theta, \theta) \quad (6)$$

Note that certain density kernels have analytic Radon transformation. For instance when $\phi(x) = \delta(x)$ the Radon transform $\mathcal{R}\phi(t, \theta) = \delta(t)$.

Radon transform of multivariate Gaussians: Let $\phi(x) = \mathcal{N}_d(\mu, \Sigma)$ be a d-dimensional multivariate Gaussian distribution with mean $\mu \in \mathbb{R}^d$ and covariance $\Sigma \in \mathbb{R}^{d \times d}$. A slice/projection of the Radon transform of ϕ is then a one-dimensional normal distribution $\mathcal{R}\phi(\cdot, \theta) = \mathcal{N}_1(\theta \cdot \mu, \theta^T \Sigma \theta)$. Given the linearity of the Radon transform, this indicates that a slice of a d-dimensional GMM is a one-dimensional GMM with component means $\theta \cdot \mu_i$ and variance $\theta^T \Sigma_i \theta$.

2.3. Sliced p -Wasserstein Distance

The idea behind the sliced p -Wasserstein distance is to first obtain a family of marginal distributions (i.e. one-dimensional distributions) for a higher-dimensional probability distribution through linear projections (via Radon transform), and then calculate the distance between two input distributions as a functional on the p -Wasserstein distance of their marginal distributions. In this sense, the distance is obtained by solving several one-dimensional optimal transport problems, which have closed-form solutions. More precisely, the Sliced Wasserstein distance between I_x and I_y is defined as,

$$SW_p(I_x, I_y) = \left(\int_{\mathbb{S}^{d-1}} W_p^p(\mathcal{R}I_x(\cdot, \theta), \mathcal{R}I_y(\cdot, \theta)) d\theta \right)^{\frac{1}{p}} \quad (7)$$

The Sliced p -Wasserstein distance as defined above is symmetric, and it satisfies sub-additivity and coincidence axioms, and hence it is a true metric [30].

The sliced p -Wasserstein distance is especially useful when one only has access to samples of a high-dimensional PDFs and kernel density estimation is required to estimate I . One dimensional kernel density estimation of PDF slices is a much simpler task compared to direct estimation of I from its samples. The catch, however, is that as the dimensionality grows one requires larger number of projections to estimate I from $\mathcal{R}I(\cdot, \theta)$. In short, if a reasonably smooth two-dimensional distribution can be approximated by its L projections (up to an acceptable reconstruction error, ϵ), then one would require $\mathcal{O}(L^{d-1})$ number of projections to approximate a similarly smooth d-dimensional distribution (for $d \geq 2$). In later sections we show that the projections could be randomized in a stochastic Gradient descent fashion for learning Gaussian mixture models.

3. Sliced Wasserstein Means and Gaussian Mixture Models

Here we first reiterate the connection between the K-means clustering algorithm and the Wasserstein means problem, and then extend this connection to GMMs and state the need for the sliced Wasserstein distance. Let $y_n \in \mathbb{R}^d$ for $n = 1, \dots, N$ be N samples and $Y = [y_1, \dots, y_N] \in \mathbb{R}^{d \times N}$. The K-means clustering algorithm seeks the best K points, $x_k \in \mathbb{R}^d$ for $k = 1, \dots, K$ and $X = [x_1, \dots, x_K] \in \mathbb{R}^{d \times K}$, that represent Y . Formally,

$$\begin{aligned} \inf_{C, X} \frac{1}{N} \|Y - XC^T\|^2 \\ \text{s.t. } C1_K = 1_N, c_{i,j} \in \{0, 1\} \end{aligned} \quad (8)$$

where $C \in \mathbb{R}^{N \times K}$ contains the one-hot labels of Y .

Let $I_y = \frac{1}{N} \sum_{n=1}^N \phi(y - y_n)$ be the empirical distribution of Y , where ϕ is a kernel density estimator (e.g. radial

basis function kernel or the Dirac delta function in its limit). Then, the K-means problem can be alternatively solved by minimizing a statistical distance/divergence between I_y and $I_x = \frac{1}{K} \sum_{k=1}^K \phi(x - x_k)$. A common choice for such distance/divergence is the Kullback-Leibler divergence (KL-divergence) [4, 10]. Alternatively, the p-Wasserstein distance could be used to estimate the parameters of I_x ,

$$\inf_{I_x} W_p^p(I_x, I_y) \quad (9)$$

We discuss the benefits of the p-Wasserstein distance over the KL-divergence in the next sub-section. Above minimization is known as the *Wasserstein means problem* and is closely related to the Wasserstein Barycenter problem [1, 46, 14, 21]. The main difference being in that in these works the goal is to find a measure ν^* such that $\nu^* = \arg \inf_{\nu} \sum_k W_p^p(\nu_k, \nu)$, where ν_k are sets of given low dimensional distributions (2 or 3D images or point clouds). The strategy in [1, 46, 14] could also be extended into a clustering problem, though the two formulations are still significantly different given the inputs into the Wasserstein distance being very different. Note also that K-means is equivalent to a variational EM approximation of a GMM with isotropic Gaussians [36], therefore, a natural extension of the *Wasserstein means problem* could be formulated to fit a general GMM to I_y . To do so, we let distribution I_x to be the parametric GMM as follows:

$$I_x(x) = \sum_k \frac{\alpha_k}{(2\pi)^{\frac{d}{2}} \sqrt{\det(\Sigma_k)}} \exp\left(-\frac{1}{2}(x - \mu_k)^T \Sigma_k^{-1}(x - \mu_k)\right)$$

where $\sum_k \alpha_k = 1$ and Equation (9) is solved to find μ_k s, Σ_k s, and α_k s. Next we describe the benefits of using the Wasserstein distance in Equation (9) to fit a general GMM to the observed data compared to the common log-likelihood maximization schemes.

3.1. Wasserstein Means vs. Maximum Log-Likelihood

General GMMs are often fitted to the observed data points, y_n s, via maximizing the log-likelihood of samples with respect to I_x . Formally, this is written as:

$$\max_{\mu_k, \Sigma_k, \alpha_k} \frac{1}{N} \sum_{n=1}^N \log(I_x(y_n)) \quad (10)$$

It is straightforward to show that in the limit and as the number of samples grows to infinity, $N \rightarrow \infty$, the maximum log-likelihood becomes equivalent to minimizing the KL-divergence between I_x and I_y (See supplementary material for a proof):

$$\lim_{N \rightarrow \infty} \max_{\mu_k, \Sigma_k, \alpha_k} \frac{1}{N} \sum_{n=1}^N \log(I_x(y_n)) = \min_{\mu_k, \Sigma_k, \alpha_k} KL(I_x, I_y)$$

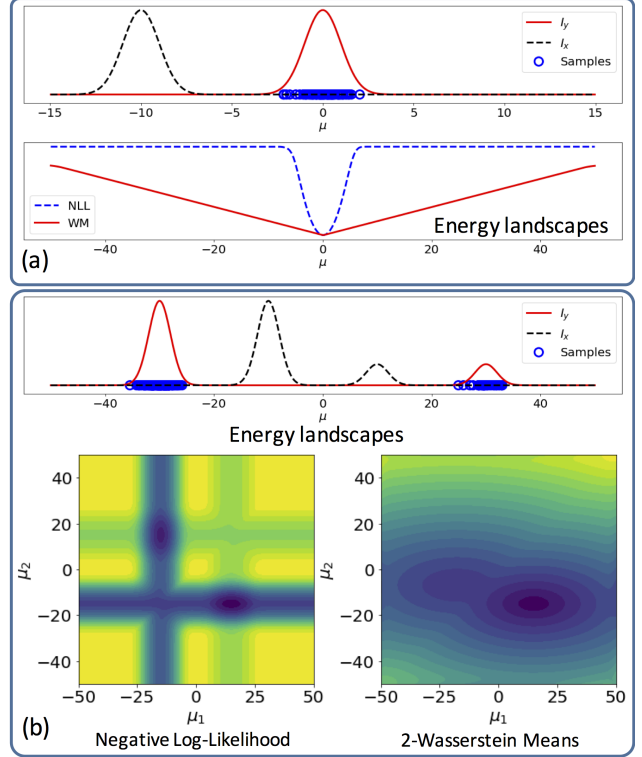


Figure 1. The corresponding energy landscapes for the negative log-likelihood and the Wasserstein Means problem for scenario 1 (a) and scenario 2 (b). The energy landscapes are scaled and shifted for visualization purposes.

The p-Wasserstein distance has been shown to have certain benefits over the commonly used KL-divergence and its related distances/divergences (i.e., other examples of Bregman divergences including the Jensen-Shannon (JS) distance and Itakura-Saito distance) [3]. For a general GMM, the model I_x is continuous and smooth (i.e. infinitely differentiable) in its parameters and is locally Lipschitz; therefore, $W_p(I_x, I_y)$ is continuous and differentiable everywhere, while this is not true for the KL-divergence. In addition, in scenarios where the distributions are supported by low dimensional manifolds, KL-divergence and other Bregman divergences may be difficult cost functions to optimize given their limited capture range. This limitation is due to their ‘Eulerian’ nature, in the sense that the distributions are compared at fixed spatial coordinates (i.e., bin-to-bin comparison in discrete measures) as opposed to the p-Wasserstein distance, which is ‘Lagrangian’, and morphs one distribution to match another by finding correspondences in the domain of these distributions (i.e., Wasserstein distances perform cross-bin comparisons).

To get a practical sense of the benefits of the Wasserstein means problem over the maximum log-likelihood estimation, we study two simple scenarios. In the first scenario, we generate N one-dimensional samples, y_n , from a normal dis-

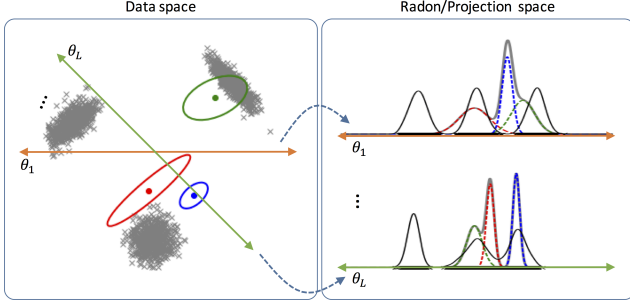


Figure 2. Illustration of the high-level approach for the Sliced Wasserstein Means of GMMs.

tribution $\mathcal{N}(0, \sigma)$ where we assume known σ and visualize the *negative log-likelihood (NLL)* and the *Wasserstein means (WM) problem* as a function of μ . Figure 1 (a) shows the first scenario and the corresponding energy landscapes for the negative log-likelihood and the Wasserstein means problem. It can be seen that while the global optimum is the same for both problems, the Wasserstein means landscape is less sensitive to the initial point, hence a gradient descent approach would easily converge to the optimal point regardless of the starting point. In the second scenario, we generated N samples, y_n , from a mixture of two one-dimensional Gaussian distributions. Next, we assumed that the mixture coefficients α_k s and the standard deviations σ_k s, for $k \in \{0, 1\}$, are known and visualized the corresponding energy landscapes for NLL and WM as a function of μ_k s (See Figure 1 (b)). It can be clearly seen that although the global optimum of both problems is the same, but the energy landscape of the Wasserstein means problem does not suffer from local minima and is much smoother.

The Wasserstein means problem, however, suffers from the fact that the $W_2^2(\cdot, \cdot)$ is computationally expensive to calculate for high-dimensional I_x and I_y . This is true even using very efficient OMT solvers, including the ones introduced by Cuturi [13], Solomon et al. [48], and Levy [32].

3.2. Sliced Wasserstein Means

We propose to use an approximation of the p-Wasserstein distance between I_x and I_y using the SW distance. Substituting the Wasserstein distance in Equation (9) with the SW distance leads to the *Sliced p-Wasserstein Means (SWM)* problem,

$$\inf_{\mu_k, \Sigma_k, \alpha_k} SW_p^p(I_x, I_y) = \int_{\mathbb{S}^{d-1}} W_p^p(\mathcal{R}I_x(\cdot, \theta), \mathcal{R}I_y(\cdot, \theta)) d\theta,$$

which can be written as:

$$\inf_{\mu_k, \Sigma_k, \alpha_k} \int_{\mathbb{S}^{d-1}} \inf_{f(\cdot, \theta)} \int_{\mathbb{R}} |f(t, \theta) - t|^p \mathcal{R}I_x(t, \theta) dt d\theta \quad (11)$$

where for a fixed θ , $f(\cdot, \theta)$ is the optimal transport map between $\mathcal{R}I_x(\cdot, \theta)$ and $\mathcal{R}I_y(\cdot, \theta)$, and satisfies

$\frac{\partial f(t, \theta)}{\partial t} \mathcal{R}I_y(f(t, \theta), \theta) = \mathcal{R}I_x(t, \theta)$. Note that, since I_x is an absolutely continuous PDF, an optimal transport map will exist even when I_y is not an absolutely continuous PDF (e.g. when $\phi(y) = \delta(y)$). Moreover, since the slices/projections are one-dimensional the transport map, $f(\cdot, \theta)$, is uniquely defined and the minimization on f has a closed form solution and is calculated from Equation (3). The Radon transformations in Equation (11) are:

$$\begin{cases} \mathcal{R}I_y(t, \theta) \approx \frac{1}{N} \sum_{n=1}^N \mathcal{R}\phi(t - y_n \cdot \theta, \theta) \\ \mathcal{R}I_x(t, \theta) = \sum_k \frac{\alpha_k}{\sqrt{2\pi\theta^T \Sigma_k \theta}} \exp\left(-\frac{(t - \mu_k \cdot \theta)^2}{2\theta^T \Sigma_k \theta}\right) \end{cases} \quad (12)$$

The new formulation avoids the optimization for calculating the Wasserstein distance and enables an efficient implementation for clustering high-dimensional data. Figure 2 demonstrates the high-level idea behind slicing high-dimensional PDFs I_x and I_y and minimizing the p-Wasserstein distance between these slices over GMM components. Moreover, given the high-dimensional nature of the problem estimating density I_y in \mathbb{R}^d requires large number of samples, however, the projections of I_y , $\mathcal{R}I_y(\cdot, \theta)$, are one dimensional and therefore it may not be critical to have large number of samples to estimate these one-dimensional densities.

Optimization scheme: To obtain a numerical optimization scheme, which minimizes the problem in Equation (11) we first discretize the set of directions/projections. This corresponds to the use of a finite set $\Theta \in \mathbb{S}^{d-1}$, and a minimization of the following energy function,

$$\inf_{\mu_k, \Sigma_k, \alpha_k} \frac{1}{|\Theta|} \sum_{l=1}^{|\Theta|} \int_{\mathbb{R}} |f(t, \theta_l) - t|^p \mathcal{R}I_x(t, \theta_l) dt \quad (13)$$

A fine sampling of \mathbb{S}^{d-1} is required for Equation (13) to be a good approximation of (11). Such sampling, however, becomes prohibitively expensive for high-dimensional data. Alternatively, following the approach presented in [6] we utilize random samples of \mathbb{S}^{d-1} at each minimization step to approximate the Equation (11). This leads to a stochastic gradient descent scheme where instead of random sampling of the input data, we random sample the projection angles. Finally, the GMM parameters are updated through an EM-like approach where for fixed GMM parameters we calculate the optimal transport map f between random slices of I_x and I_y , followed by updating I_x for fixed transport maps $f(\cdot, \theta)$ s. Below we describe these steps:

1. Generate L random samples from $\mathbb{S}^{(d-1)}$, $\{\theta_1, \dots, \theta_L\}$.
2. Fix the GMM, I_x , and calculate the optimal transport map between slices $\mathcal{R}I_x(\cdot, \theta_l)$ and $\mathcal{R}I_y(\cdot, \theta_l)$ via:

$$f(t, \theta_l) = \mathcal{R}J_y^{-1}(\mathcal{R}J_x(t, \theta_l), \theta_l) \quad (14)$$

where $\mathcal{R}J_{x(y)}(\cdot, \theta_l)$ is the CDF of $\mathcal{R}I_{x(y)}(\cdot, \theta_l)$.

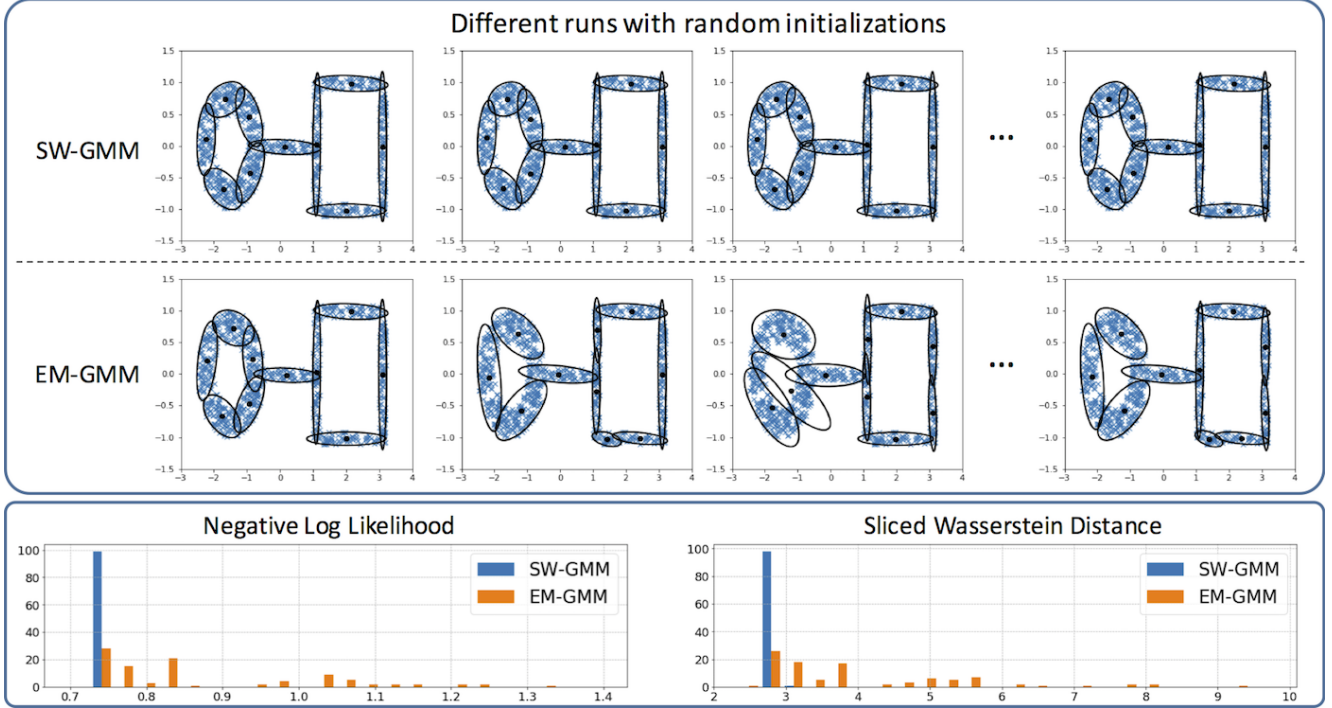


Figure 3. Results of 100 runs of EM-GMM and SW-GMM fitting a model with 10 modes to the ring-line-square dataset, showing four samples of random initializations (Top) and histograms across all 100 runs for the negative log-likelihood of the fitted model and the sliced-Wasserstein distance between the fitted model and the data distribution (Bottom).

3. For fixed transportmaps, $f(\cdot, \theta_l)$ s, update the GMM parameters by differentiating Equation (11):

$$\begin{aligned} \frac{\partial SW_p^p}{\partial \alpha_k} &= \sum_{l=1}^L \int_{\mathbb{R}} \frac{|f(t, \theta_l) - t|^p}{\sqrt{2\pi\theta_l^T \Sigma_k \theta_l}} \exp\left(-\frac{(t - \mu_k \cdot \theta_l)^2}{2\theta_l^T \Sigma_k \theta_l}\right) dt \\ \frac{\partial SW_p^p}{\partial \mu_k} &= \sum_{l=1}^L \left(\int_{\mathbb{R}} \frac{\alpha_k |f(t, \theta_l) - t|^p}{\sqrt{2\pi\theta_l^T \Sigma_k \theta_l}} \exp\left(-\frac{(t - \mu_k \cdot \theta_l)^2}{2\theta_l^T \Sigma_k \theta_l}\right) \right. \\ &\quad \left. \frac{(t - \mu_k \cdot \theta_l)}{\theta_l^T \Sigma_k \theta_l} dt \right) \theta_l \\ \frac{\partial SW_p^p}{\partial \Sigma_k} &= \sum_{l=1}^L \left(\int_{\mathbb{R}} \frac{\alpha_k |f(t, \theta_l) - t|^p}{\sqrt{8\pi(\theta_l^T \Sigma_k \theta_l)^3}} \left[\frac{(t - \mu_k \cdot \theta_l)^2}{\theta_l^T \Sigma_k \theta_l} - 1 \right] \right. \\ &\quad \left. \exp\left(-\frac{(t - \mu_k \cdot \theta_l)^2}{2\theta_l^T \Sigma_k \theta_l}\right) dt \right) (\theta_l \theta_l^T) \end{aligned}$$

where the summation is over L random projections $\theta_l \in \mathbb{S}^{d-1}$. We use the RMSProp optimizer [50], which provides an adaptive learning rate, to update the parameters of the GMM according to the gradients

4. Project the updated Σ_k s onto the positive semidefinite cone, and renormalize α_k s to satisfy $\sum_k \alpha_k = 1$.

Notice that the derivative with respect to the k 'th component of the mixture model in Equation (15) is independent of other components. In addition, the transport map for each projection, $f(\cdot, \theta)$, in Equation (14) is calculated independent of the other projections. Therefore the optimization can

be heavily parallelized in each iteration. We note that, we have also experimented with the Adam optimizer [27] but did not see any improvements over RMSProp. The detailed update equations are included in the Supplementary materials. In what follows we show the SWM solver for estimating GMM parameters in action.

4. Numerical Experiments

We ran various experiments on three datasets to test our proposed method for learning GMM parameters. The first dataset is a two-dimensional data-point distribution consisting of a ring, a square, and a connecting line (See Figure 3). To show the applicability of our method on higher-dimensional datasets we also used the MNIST dataset [31] and the CelebFaces Attributes Dataset (CelebA) [35].

4.1. Robustness to initialization

We started by running a simple experiment to demonstrate the robustness of our proposed formulation to different initializations. In this test, we used a two-dimensional dataset consisting of a ring, a square, and a line connecting them. For a fixed number of modes, $K = 10$ in our experiment, we randomly initialized the GMM. Next, for each initialization, we optimized the GMM parameters using the EM algorithm as well as our proposed method. We repeated this experiment 100 times.

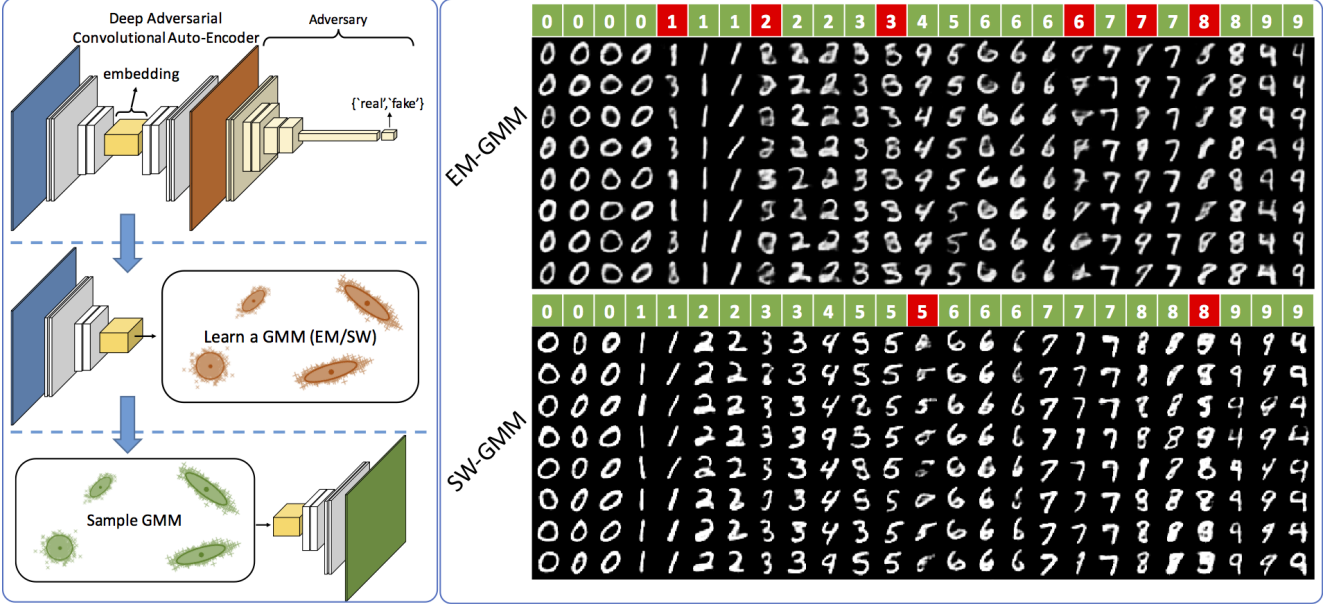


Figure 4. Qualitative performance comparison on the MNIST dataset between our method, SW-GMM, and EM-GMM, showing decoded samples for each mode (Right). Modes with bad samples are shown in red. The GMM was applied to a 128-dimensional embedding space (Left).

Figure 3 shows sample results of the fitted GMM models for both algorithms (Top Row). Moreover, we calculated the histograms of the negative log-likelihood of the fitted GMM and the sliced-Wasserstein distance between the fitted GMM and the empirical data distribution (bottom). It can be seen that our proposed formulation provides a consistent model regardless of the initialization. In 100% of initializations, our method achieved the optimal negative log-likelihood, compared to only 29% for EM-GMM. In addition, both the negative log-likelihood and the sliced-Wasserstein distance for our method are smaller than those of the EM algorithm, indicating that our solution is closer to the global optimum (up to permutations of the modes).

4.2. High-dimensional datasets

We analyzed the performance of our proposed method in modeling high-dimensional data distributions, here, using the MNIST dataset [31] and the CelebA dataset [35]. To capture the nonlinearity of the image data and boost the applicability of GMMs, we trained an adversarial deep convolutional autoencoder (Figure 4, Left) on the image data. Next, we modeled the distribution of the data in the embedded space via a GMM. The GMM was then used to generate samples in the embedding space, which were consequently decoded to generate synthetic (i.e. 'fake') images. In learning the GMM, we compared the EM algorithm with our proposed method, SW-GMM. We note that the entire pipeline is in an unsupervised learning setting. Figure 4 demonstrates the steps of our experiment (Left) and provides

a qualitative measure of the generated samples (Right) for the MNIST dataset. It can be seen that the SW-GMM model leads to more visually appealing samples compared to the EM-GMM. In addition, we trained a CNN classifier on the MNIST training data. We then generated 10,000 samples from each GMM component and classified these samples to measure the fidelity/pureness of each component. Ideally, each component should only be assigned to a single digit. We found out that for EM-GMM the components were in average 80.48% pure, compared to 86.98% pureness of SW-GMM components.

Similarly, a deep convolutional autoencoder was learned for the CelebA face dataset, and a GMM was trained in the embedding space. Figure 5 shows samples generated from GMM components learned by EM and by our proposed method (The samples generated from all components is attached in the Supplementary materials). We note that, Figures 4 and 5 only provide qualitative measures of how well the GMM is fitting the dataset. Next we provide quantitative measures for the fitness of the GMMs for both methods.

We used adversarial training of neural networks [18, 33] to provide a goodness of fitness of the GMM to the data distribution. In short, we use success in fooling an adversary network as an evaluation metric for goodness of fit of a GMM. A deep discriminator/classifier was trained to distinguish whether a data point was sampled from the actual data distribution or from the GMM. The fooling rate (i.e. error rate) of such a discriminator is a good measure of fitness for the GMM, as a higher error rate translates to a better fit to

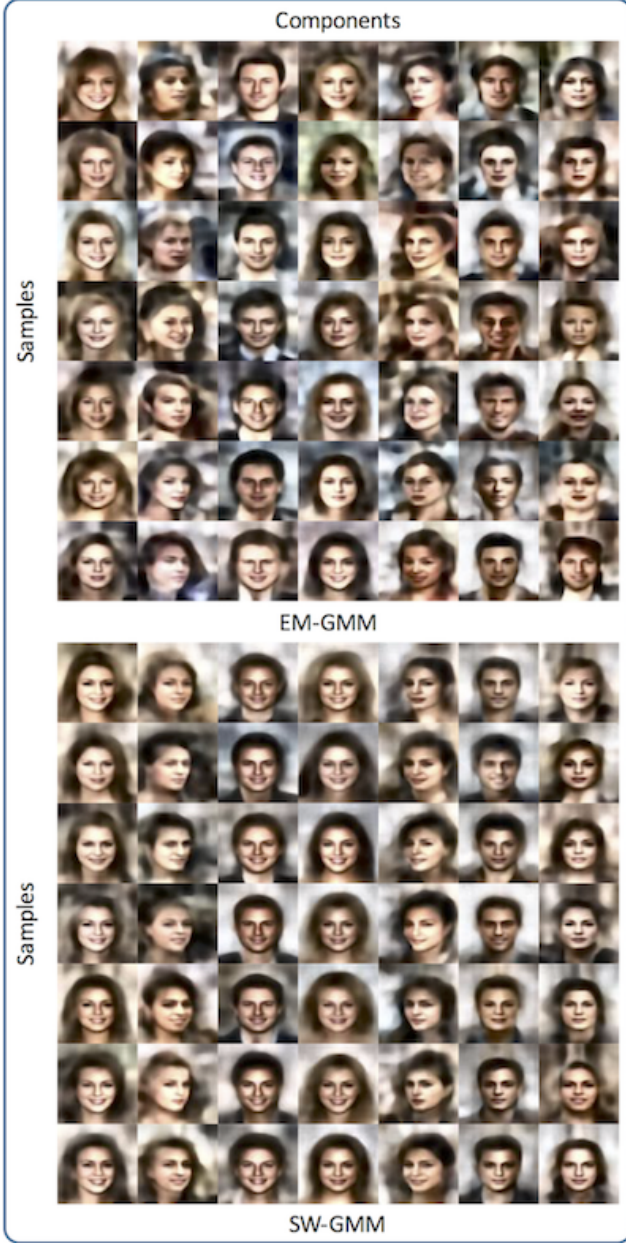
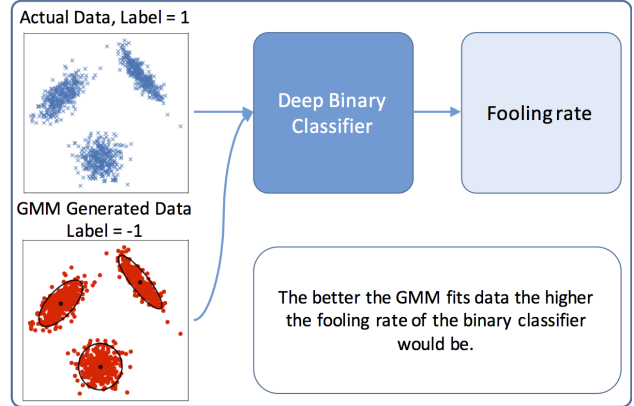


Figure 5. Qualitative performance comparison between our method, SW-GMM (Bottom), and EM-GMM (Top), showing decoded samples for several GMM components. The images are contrast enhanced for visualization purposes.

the distribution of the data. Figure 6 shows the idea behind this experiment, and reports the fooling rates for all three datasets used in our experiments. Note that the SW-GMM consistently provides a higher fooling rate, indicating a better fit to the datasets. Moreover, we point out that while for the low-dimensional ring-square-line dataset both methods provide reasonable models for the dataset, the SW-GMM significantly outperforms EM-GMM for higher-dimensional



Fooling rate	EM-GMM	SW-GMM
Ring-Square-Line	46.83% \pm 1.14%	47.56% \pm 0.86%
MNIST	24.87% \pm 8.39%	41.91% \pm 2.35%
CelebA	10.37% \pm 3.22%	31.83% \pm 1.24%

Figure 6. A deep discriminator is learned to classify whether an input is sampled from the true distribution of the data or via the GMM. The fooling rate of such a discriminator corresponds to the fitness score of the GMM.

datasets (i.e. the MNIST and CelebA datasets).

The details of the architectures used in our experiments are included in the supplementary material.

5. Discussion

In this paper, we proposed a novel algorithm for estimating the parameters of a GMM via minimization of the sliced p-Wasserstein distance. In each iteration, our method projects the high-dimensional data distribution into a small set of one-dimensional distributions utilizing random projections/slices of the Radon transform and estimates the GMM parameters from these one-dimensional projections. While we did not provide a theoretical guarantee that the new method is convex, or that it has fewer local minima, the empirical results suggest that our method is more robust compared to KL-divergence-based methods, including the EM algorithm, for maximizing the log-likelihood function. Consistent with this finding, we showed that the p-Wasserstein metrics result in more well-behaved energy landscapes. We demonstrated the robustness of our method on three datasets: a two-dimensional ring-square-line distribution and the high-dimensional MNIST and CelebA face datasets. Finally, while we used deep convolutional encoders to provide embeddings for two of the datasets and learned GMMs in these embeddings, we emphasize that our method could be applied to other embeddings including the original data space.

6. Acknowledgement

This work was partially supported by NSF (CCF 1421502). The authors gratefully appreciate countless fruitful conversations with Drs. Charles H. Martin and Dejan Slepčev.

References

- [1] M. Agueh and G. Carlier. Barycenters in the Wasserstein space. *SIAM Journal on Mathematical Analysis*, 43(2):904–924, 2011. 4
- [2] C. Améndola, M. Drton, and B. Sturmfels. Maximum likelihood estimates for gaussian mixtures are transcendental. In *International Conference on Mathematical Aspects of Computer and Information Sciences*, pages 579–590. Springer, 2015. 1
- [3] M. Arjovsky, S. Chintala, and L. Bottou. Wasserstein generative adversarial networks. In *International Conference on Machine Learning*, pages 214–223, 2017. 1, 2, 4
- [4] A. Banerjee, S. Merugu, I. S. Dhillon, and J. Ghosh. Clustering with bregman divergences. *Journal of machine learning research*, 6(Oct):1705–1749, 2005. 4
- [5] C. Beecks, A. M. Ivanescu, S. Kirchhoff, and T. Seidl. Modeling image similarity by gaussian mixture models and the signature quadratic form distance. In *Computer Vision (ICCV), 2011 IEEE International Conference On*, pages 1754–1761. IEEE, 2011. 1
- [6] N. Bonneel, J. Rabin, G. Peyré, and H. Pfister. Sliced and Radon Wasserstein barycenters of measures. *Journal of Mathematical Imaging and Vision*, 51(1):22–45, 2015. 2, 3, 5
- [7] Y. Brenier. Polar factorization and monotone rearrangement of vector-valued functions. *Communications on pure and applied mathematics*, 44(4):375–417, 1991. 2
- [8] W. M. Campbell, D. E. Sturim, and D. A. Reynolds. Support vector machines using gmm supervectors for speaker verification. *IEEE signal processing letters*, 13(5):308–311, 2006. 1
- [9] T. Celik and T. Tjahjadi. Automatic image equalization and contrast enhancement using gaussian mixture modeling. *IEEE Transactions on Image Processing*, 21(1):145–156, 2012. 1
- [10] K. Chaudhuri and A. McGregor. Finding metric structure in information theoretic clustering. In *COLT*, volume 8, page 10, 2008. 4
- [11] Y. Chen, T. T. Georgiou, and A. Tannenbaum. Optimal transport for gaussian mixture models. *arXiv preprint arXiv:1710.07876*, 2017. 2
- [12] F. Chollet et al. Keras. <https://github.com/fchollet/keras>, 2015. 11
- [13] M. Cuturi. Sinkhorn distances: Lightspeed computation of optimal transport. In *Advances in Neural Information Processing Systems*, pages 2292–2300, 2013. 5
- [14] M. Cuturi and A. Doucet. Fast computation of wasserstein barycenters. In *International Conference on Machine Learning*, pages 685–693, 2014. 4
- [15] A. P. Dempster, N. M. Laird, and D. B. Rubin. Maximum likelihood from incomplete data via the em algorithm. *Journal of the royal statistical society. Series B (methodological)*, pages 1–38, 1977. 1
- [16] C. Frogner, C. Zhang, H. Mobahi, M. Araya, and T. A. Poggio. Learning with a wasserstein loss. In *Advances in Neural Information Processing Systems*, pages 2053–2061, 2015. 1
- [17] J. Goldberger, S. Gordon, and H. Greenspan. An efficient image similarity measure based on approximations of kl-divergence between two gaussian mixtures. In *null*, page 487. IEEE, 2003. 1
- [18] I. Goodfellow, J. Pouget-Abadie, M. Mirza, B. Xu, D. Warde-Farley, S. Ozair, A. Courville, and Y. Bengio. Generative adversarial nets. In *Advances in neural information processing systems*, pages 2672–2680, 2014. 7
- [19] J. A. Guerrero-Colón, L. Mancera, and J. Portilla. Image restoration using space-variant gaussian scale mixtures in overcomplete pyramids. *IEEE Transactions on Image Processing*, 17(1):27–41, 2008. 1
- [20] I. Gulrajani, F. Ahmed, M. Arjovsky, V. Dumoulin, and A. Courville. Improved training of wasserstein gans. *arXiv preprint arXiv:1704.00028*, 2017. 1
- [21] N. Ho, X. Nguyen, M. Yurochkin, H. H. Bui, V. Huynh, and D. Phung. Multilevel clustering via wasserstein means. *arXiv preprint arXiv:1706.03883*, 2017. 2, 4
- [22] H. Hoffmann. *Unsupervised Learning of Visuomotor Associations*, volume 11 of *MPI Series in Biological Cybernetics*. Logos Verlag Berlin, 2005. 1
- [23] H. Hoffmann, W. Schenck, and R. Möller. Learning visuomotor transformations for gaze-control and grasping. *Biological Cybernetics*, 93:119–130, 2005. 1
- [24] B. Jian and B. C. Vemuri. Robust point set registration using gaussian mixture models. *IEEE Transactions on Pattern Analysis and Machine Intelligence*, 33(8):1633–1645, 2011. 1
- [25] C. Jin, Y. Zhang, S. Balakrishnan, M. J. Wainwright, and M. I. Jordan. Local maxima in the likelihood of gaussian mixture models: Structural results and algorithmic consequences. In *Advances in Neural Information Processing Systems*, pages 4116–4124, 2016. 1
- [26] A. T. Kalai, A. Moitra, and G. Valiant. Disentangling gaussians. *Communications of the ACM*, 55(2):113–120, 2012. 2
- [27] D. Kingma and J. Ba. Adam: A method for stochastic optimization. *arXiv preprint arXiv:1412.6980*, 2014. 6
- [28] S. Kolouri, S. R. Park, M. Thorpe, D. Slepcev, and G. K. Rohde. Optimal mass transport: Signal processing and machine-learning applications. *IEEE Signal Processing Magazine*, 34(4):43–59, 2017. 1, 2
- [29] S. Kolouri and G. K. Rohde. Transport-based single frame super resolution of very low resolution face images. In *Proceedings of the IEEE Conference on Computer Vision and Pattern Recognition*, pages 4876–4884, 2015. 2
- [30] S. Kolouri, Y. Zou, and G. K. Rohde. Sliced-Wasserstein kernels for probability distributions. In *Proceedings of the IEEE Conference on Computer Vision and Pattern Recognition*, pages 4876–4884, 2016. 2, 3
- [31] Y. LeCun. The mnist database of handwritten digits. <http://yann.lecun.com/exdb/mnist/>. 6, 7

- [32] B. Lévy. A numerical algorithm for L_2 semi-discrete optimal transport in 3D. *ESAIM Math. Model. Numer. Anal.*, 49(6):1693–1715, 2015. [5](#)
- [33] J. Li, W. Monroe, T. Shi, A. Ritter, and D. Jurafsky. Adversarial learning for neural dialogue generation. *arXiv preprint arXiv:1701.06547*, 2017. [7](#)
- [34] P. Li, Q. Wang, and L. Zhang. A novel earth mover’s distance methodology for image matching with gaussian mixture models. In *Proceedings of the IEEE International Conference on Computer Vision*, pages 1689–1696, 2013. [2](#)
- [35] Z. Liu, P. Luo, X. Wang, and X. Tang. Deep learning face attributes in the wild. In *Proceedings of International Conference on Computer Vision (ICCV)*, 2015. [6](#), [7](#)
- [36] J. Lücke and D. Forster. k-means is a variational em approximation of gaussian mixture models. *arXiv preprint arXiv:1704.04812*, 2017. [4](#)
- [37] G. J. McLachlan and S. Rathnayake. On the number of components in a gaussian mixture model. *Wiley Interdisciplinary Reviews: Data Mining and Knowledge Discovery*, 4(5):341–355, 2014. [1](#)
- [38] R. Möller and H. Hoffmann. An extension of neural gas to local PCA. *Neurocomputing*, 62:305–326, 2004. [1](#)
- [39] G. Montavon, K.-R. Müller, and M. Cuturi. Wasserstein training of restricted boltzmann machines. In *Advances in Neural Information Processing Systems*, pages 3718–3726, 2016. [1](#)
- [40] K. P. Murphy. *Machine learning: a probabilistic perspective*. MIT press, 2012. [1](#)
- [41] F. Natterer. *The mathematics of computerized tomography*, volume 32. Siam, 1986. [3](#)
- [42] S. R. Park, S. Kolouri, S. Kundu, and G. K. Rohde. The cumulative distribution transform and linear pattern classification. *Applied and Computational Harmonic Analysis*, 2017. [2](#)
- [43] H. Permuter, J. Francos, and I. Jermyn. A study of gaussian mixture models of color and texture features for image classification and segmentation. *Pattern Recognition*, 39(4):695–706, 2006. [1](#)
- [44] G. Peyré, J. Fadili, and J. Rabin. Wasserstein active contours. In *Image Processing (ICIP), 2012 19th IEEE International Conference on*, pages 2541–2544. IEEE, 2012. [1](#)
- [45] Y. Qian, E. Vazquez, and B. Sengupta. Deep geometric retrieval. *arXiv preprint arXiv:1702.06383*, 2017. [2](#)
- [46] J. Rabin, G. Peyré, J. Delon, and M. Bernot. Wasserstein barycenter and its application to texture mixing. In *Scale Space and Variational Methods in Computer Vision*, pages 435–446. Springer, 2012. [4](#)
- [47] A. Rolet, M. Cuturi, and G. Peyré. Fast dictionary learning with a smoothed wasserstein loss. In *Artificial Intelligence and Statistics*, pages 630–638, 2016. [2](#)
- [48] J. Solomon, F. de Goes, P. A. Studios, G. Peyré, M. Cuturi, A. Butscher, A. Nguyen, T. Du, and L. Guibas. Convolutional Wasserstein distances: Efficient optimal transportation on geometric domains. *ACM Transactions on Graphics (Proc. SIGGRAPH 2015)*, to appear, 2015. [5](#)
- [49] M. Thorpe, S. Park, S. Kolouri, G. K. Rohde, and D. Slepčev. A transportation ℓ^p distance for signal analysis. *Journal of Mathematical Imaging and Vision*, 59(2):187–210, 2017. [2](#)
- [50] T. Tieleman and G. Hinton. Lecture 6.5-rmsprop: Divide the gradient by a running average of its recent magnitude. *COURSERA: Neural networks for machine learning*, 4(2):26–31, 2012. [6](#), [11](#)
- [51] M. E. Tipping and C. M. Bishop. Mixtures of probabilistic principal component analyzers. *Neural Computation*, 11:443–482, 1999. [1](#)
- [52] S. S. Vempala. *The random projection method*, volume 65. American Mathematical Soc., 2005. [2](#)
- [53] C. Villani. *Optimal transport: old and new*, volume 338. Springer Science & Business Media, 2008. [2](#)
- [54] S. Xiao, M. Farajtabar, X. Ye, J. Yan, L. Song, and H. Zha. Wasserstein learning of deep generative point process models. *arXiv preprint arXiv:1705.08051*, 2017. [2](#)
- [55] G. Yu, G. Sapiro, and S. Mallat. Solving inverse problems with piecewise linear estimators: From gaussian mixture models to structured sparsity. *IEEE Transactions on Image Processing*, 21(5):2481–2499, 2012. [1](#)

7. Supplementary material

7.1. Maximum log-likelihood and KL-divergence

The KL-divergence between I_x and I_y is defined as:

$$KL(I_x, I_y) = \int_{\mathbb{R}^d} I_y(\rho) \log\left(\frac{I_y(\rho)}{I_x(\rho)}\right) d\rho$$

For the maximum log-likelihood and in the limit and as the number of samples grows to infinity, $N \rightarrow \infty$, we have:

$$\begin{aligned} \lim_{N \rightarrow \infty} \operatorname{argmax}_{\mu_k, \Sigma_k, \alpha_k} \frac{1}{N} \sum_{n=1}^N \log(I_x(y_n)) &= \\ \operatorname{argmax}_{\mu_k, \Sigma_k, \alpha_k} \int_{\mathbb{R}^d} I_y(\rho) \log(I_x(\rho)) d\rho &= \\ \operatorname{argmin}_{\mu_k, \Sigma_k, \alpha_k} - \int_{\mathbb{R}^d} I_y(\rho) \log(I_x(\rho)) d\rho &= \\ \operatorname{argmin}_{\mu_k, \Sigma_k, \alpha_k} \int_{\mathbb{R}^d} I_y(\rho) \log(I_y(\rho)) d\rho - & \\ \int_{\mathbb{R}^d} I_y(\rho) \log(I_x(\rho)) d\rho &= \\ \operatorname{argmin}_{\mu_k, \Sigma_k, \alpha_k} \int_{\mathbb{R}^d} I_y(\rho) \log\left(\frac{I_y(\rho)}{I_x(\rho)}\right) d\rho &= \\ \operatorname{argmin}_{\mu_k, \Sigma_k, \alpha_k} KL(I_x, I_y) & \end{aligned}$$

7.2. RMSProp update equations

SGD often suffers from oscillatory behavior across the slopes of a ravine while only making incremental progress towards the optimal point. Various momentum based methods have been introduced to adaptively change the learning rate of SGD and dampen this oscillatory behavior. In our work, we used RMSProp, introduced by Tieleman and Hinton [50], which is a momentum based technique for SGD. Let α be the learning rate, $\gamma \in (0, 1)$ be the decay parameter, and κ be the momentum parameter. The update equation for a GMM parameter, here μ_k , is then calculated from:

$$\begin{cases} m_k^{(i)} = \gamma m_k^{(i-1)} + (1 - \gamma) \frac{\partial SW_p^p(I_x, I_y)}{\partial \mu_k} \\ g_k^{(i)} = \gamma g_k^{(i-1)} + (1 - \gamma) \left(\frac{\partial SW_p^p(I_x, I_y)}{\partial \mu_k} \right)^2 \\ v_k^{(i)} = \kappa v_k^{(i-1)} - \frac{\alpha}{\sqrt{g_k^{(i)} - (m_k^{(i)} - m_k^{(i-1)})^2 + \epsilon}} \frac{\partial SW_p^p(I_x, I_y)}{\partial \mu_k} \\ \mu_k^{(i)} = \mu_k^{(i-1)} + v_k^{(i)} \end{cases} \quad (15)$$

Where m_k and g_k are the first and second moments (uncentered variance) of $\partial SW_p^p(I_x, I_y) / \partial \mu_k$, respectively. Similar update equations hold for Σ_k and α_k .

7.3. Experimental Details

Here we provide the detailed implementation and architecture of the adversarial autoencoders we used in our paper. Figure 8 shows the detailed architectures of the deep adversarial autoencoder for MNIST and CelebA datasets. The architecture of the deep binary classifiers used for scoring the fitness of the GMMs are shown in Figure 7. We used Keras [12] for implementation of our experiments.

For the loss function of the autoencoder we used the *mean absolute error* between the input image and the decoded image together with the adversarial loss of the decoded image (equally weighted). The loss functions for training the adversarial networks and the binary classifiers were chosen to be cross entropy. Finally, we used RMSProp [50] as the default optimizer for all the models, and trained the models over 100 Epochs, with batch size of 250.

7.4. CelebA Generated Images

Figure 9 shows all the GMM components learned by EM and our SWM formulation.

MNIST Dataset

Layer (type)	Output Shape	Param #
input_1 (InputLayer)	(None, 28, 28, 1)	0
conv2d_1 (Conv2D)	(None, 28, 28, 8)	80
leaky_re_lu_1 (LeakyReLU)	(None, 28, 28, 8)	0
conv2d_2 (Conv2D)	(None, 28, 28, 8)	584
leaky_re_lu_2 (LeakyReLU)	(None, 28, 28, 8)	0
max_pooling2d_1 (MaxPooling2)	(None, 14, 14, 8)	0
conv2d_3 (Conv2D)	(None, 14, 14, 16)	1168
leaky_re_lu_3 (LeakyReLU)	(None, 14, 14, 16)	0
conv2d_4 (Conv2D)	(None, 14, 14, 16)	2320
leaky_re_lu_4 (LeakyReLU)	(None, 14, 14, 16)	0
max_pooling2d_2 (MaxPooling2)	(None, 7, 7, 16)	0
conv2d_5 (Conv2D)	(None, 7, 7, 32)	4640
leaky_re_lu_5 (LeakyReLU)	(None, 7, 7, 32)	0
conv2d_6 (Conv2D)	(None, 7, 7, 32)	9248
leaky_re_lu_6 (LeakyReLU)	(None, 7, 7, 32)	0
max_pooling2d_3 (MaxPooling2)	(None, 4, 4, 32)	0
flatten_1 (Flatten)	(None, 512)	0
dense_1 (Dense)	(None, 2)	1026
Total params: 19,066		
Trainable params: 19,066		
Non-trainable params: 0		

Adversarial Network

Layer (type)	Output Shape	Param #
input_1 (InputLayer)	(None, 28, 28, 1)	0
conv2d_7 (Conv2D)	(None, 28, 28, 8)	80
leaky_re_lu_7 (LeakyReLU)	(None, 28, 28, 8)	0
conv2d_8 (Conv2D)	(None, 28, 28, 8)	584
leaky_re_lu_8 (LeakyReLU)	(None, 28, 28, 8)	0
average_pooling2d_1 (Average)	(None, 14, 14, 8)	0
conv2d_9 (Conv2D)	(None, 14, 14, 16)	1168
leaky_re_lu_9 (LeakyReLU)	(None, 14, 14, 16)	0
conv2d_10 (Conv2D)	(None, 14, 14, 16)	2320
leaky_re_lu_10 (LeakyReLU)	(None, 14, 14, 16)	0
average_pooling2d_2 (Average)	(None, 7, 7, 16)	0
conv2d_11 (Conv2D)	(None, 7, 7, 32)	4640
leaky_re_lu_11 (LeakyReLU)	(None, 7, 7, 32)	0
conv2d_12 (Conv2D)	(None, 7, 7, 32)	9248
leaky_re_lu_12 (LeakyReLU)	(None, 7, 7, 32)	0
average_pooling2d_3 (Average)	(None, 4, 4, 32)	0
flatten_2 (Flatten)	(None, 512)	0
dense_2 (Dense)	(None, 128)	65664
Total params: 83,704		
Trainable params: 83,704		
Non-trainable params: 0		

Encoder

Layer (type)	Output Shape	Param #
input_2 (InputLayer)	(None, 128)	0
dense_3 (Dense)	(None, 512)	66048
reshape_1 (Reshape)	(None, 4, 4, 32)	0
conv2d_13 (Conv2D)	(None, 4, 4, 32)	9248
leaky_re_lu_13 (LeakyReLU)	(None, 4, 4, 32)	0
conv2d_14 (Conv2D)	(None, 4, 4, 32)	9248
leaky_re_lu_14 (LeakyReLU)	(None, 4, 4, 32)	0
up_sampling2d_1 (UpSampling2)	(None, 8, 8, 32)	0
conv2d_15 (Conv2D)	(None, 8, 8, 32)	9248
leaky_re_lu_15 (LeakyReLU)	(None, 8, 8, 32)	0
conv2d_16 (Conv2D)	(None, 8, 8, 32)	9248
leaky_re_lu_16 (LeakyReLU)	(None, 8, 8, 32)	0
up_sampling2d_2 (UpSampling2)	(None, 16, 16, 32)	0
conv2d_17 (Conv2D)	(None, 14, 14, 16)	4624
leaky_re_lu_17 (LeakyReLU)	(None, 14, 14, 16)	0
conv2d_18 (Conv2D)	(None, 14, 14, 16)	2320
leaky_re_lu_18 (LeakyReLU)	(None, 14, 14, 16)	0
up_sampling2d_3 (UpSampling2)	(None, 28, 28, 16)	0
conv2d_19 (Conv2D)	(None, 28, 28, 1)	145
Total params: 110,129		
Trainable params: 110,129		
Non-trainable params: 0		

Decoder

CelebA Dataset

Layer (type)	Output Shape	Param #
input_1 (InputLayer)	(None, 64, 64, 3)	0
conv2d_1 (Conv2D)	(None, 64, 64, 16)	448
leaky_re_lu_1 (LeakyReLU)	(None, 64, 64, 16)	0
conv2d_2 (Conv2D)	(None, 64, 64, 16)	2320
leaky_re_lu_2 (LeakyReLU)	(None, 64, 64, 16)	0
max_pooling2d_1 (MaxPooling2)	(None, 32, 32, 16)	0
conv2d_3 (Conv2D)	(None, 32, 32, 32)	4640
leaky_re_lu_3 (LeakyReLU)	(None, 32, 32, 32)	0
conv2d_4 (Conv2D)	(None, 32, 32, 32)	9248
leaky_re_lu_4 (LeakyReLU)	(None, 32, 32, 32)	0
max_pooling2d_2 (MaxPooling2)	(None, 16, 16, 32)	0
conv2d_5 (Conv2D)	(None, 16, 16, 64)	18496
leaky_re_lu_5 (LeakyReLU)	(None, 16, 16, 64)	0
conv2d_6 (Conv2D)	(None, 16, 16, 64)	36928
leaky_re_lu_6 (LeakyReLU)	(None, 16, 16, 64)	0
max_pooling2d_3 (MaxPooling2)	(None, 8, 8, 64)	0
conv2d_7 (Conv2D)	(None, 8, 8, 64)	36928
leaky_re_lu_7 (LeakyReLU)	(None, 8, 8, 64)	0
conv2d_8 (Conv2D)	(None, 8, 8, 64)	36928
leaky_re_lu_8 (LeakyReLU)	(None, 8, 8, 64)	0
max_pooling2d_4 (MaxPooling2)	(None, 4, 4, 64)	0
flatten_1 (Flatten)	(None, 1024)	0
dense_1 (Dense)	(None, 2)	2050
Total params: 147,986		
Trainable params: 147,986		
Non-trainable params: 0		

Adversarial Network

Layer (type)	Output Shape	Param #
input_1 (InputLayer)	(None, 64, 64, 3)	0
conv2d_9 (Conv2D)	(None, 64, 64, 16)	448
leaky_re_lu_9 (LeakyReLU)	(None, 64, 64, 16)	0
conv2d_10 (Conv2D)	(None, 64, 64, 16)	2320
leaky_re_lu_10 (LeakyReLU)	(None, 64, 64, 16)	0
average_pooling2d_1 (Average)	(None, 32, 32, 16)	0
conv2d_11 (Conv2D)	(None, 32, 32, 32)	4640
leaky_re_lu_11 (LeakyReLU)	(None, 32, 32, 32)	0
conv2d_12 (Conv2D)	(None, 32, 32, 32)	9248
leaky_re_lu_12 (LeakyReLU)	(None, 32, 32, 32)	0
average_pooling2d_2 (Average)	(None, 16, 16, 32)	0
conv2d_13 (Conv2D)	(None, 16, 16, 64)	18496
leaky_re_lu_13 (LeakyReLU)	(None, 16, 16, 64)	0
conv2d_14 (Conv2D)	(None, 16, 16, 64)	36928
leaky_re_lu_14 (LeakyReLU)	(None, 16, 16, 64)	0
average_pooling2d_3 (Average)	(None, 8, 8, 64)	0
conv2d_15 (Conv2D)	(None, 8, 8, 64)	36928
leaky_re_lu_15 (LeakyReLU)	(None, 8, 8, 64)	0
conv2d_16 (Conv2D)	(None, 8, 8, 64)	36928
leaky_re_lu_16 (LeakyReLU)	(None, 8, 8, 64)	0
average_pooling2d_4 (Average)	(None, 4, 4, 64)	0
flatten_2 (Flatten)	(None, 1024)	0
dense_2 (Dense)	(None, 256)	262400
Total params: 408,336		
Trainable params: 408,336		
Non-trainable params: 0		

Encoder

Layer (type)	Output Shape	Param #
input_2 (InputLayer)	(None, 256)	0
dense_3 (Dense)	(None, 1024)	263168
leaky_re_lu_17 (LeakyReLU)	(None, 1024)	0
reshape_1 (Reshape)	(None, 4, 4, 64)	0
conv2d_17 (Conv2D)	(None, 4, 4, 64)	36928
leaky_re_lu_18 (LeakyReLU)	(None, 4, 4, 64)	0
conv2d_18 (Conv2D)	(None, 4, 4, 64)	36928
leaky_re_lu_19 (LeakyReLU)	(None, 4, 4, 64)	0
up_sampling2d_1 (UpSampling2)	(None, 8, 8, 64)	0
conv2d_19 (Conv2D)	(None, 8, 8, 64)	36928
leaky_re_lu_20 (LeakyReLU)	(None, 8, 8, 64)	0
conv2d_20 (Conv2D)	(None, 8, 8, 64)	36928
leaky_re_lu_21 (LeakyReLU)	(None, 8, 8, 64)	0
up_sampling2d_2 (UpSampling2)	(None, 16, 16, 64)	0
conv2d_21 (Conv2D)	(None, 16, 16, 32)	18464
leaky_re_lu_22 (LeakyReLU)	(None, 16, 16, 32)	0
conv2d_22 (Conv2D)	(None, 16, 16, 32)	9248
leaky_re_lu_23 (LeakyReLU)	(None, 16, 16, 32)	0
up_sampling2d_3 (UpSampling2)	(None, 32, 32, 32)	0
conv2d_23 (Conv2D)	(None, 32, 32, 16)	4624
leaky_re_lu_24 (LeakyReLU)	(None, 32, 32, 16)	0
conv2d_24 (Conv2D)	(None, 32, 32, 16)	2320
leaky_re_lu_25 (LeakyReLU)	(None, 32, 32, 16)	0
up_sampling2d_4 (UpSampling2)	(None, 64, 64, 16)	0
conv2d_25 (Conv2D)	(None, 64, 64, 3)	435
Total params: 445,971		
Trainable params: 445,971		
Non-trainable params: 0		

Decoder

Figure 7. Details of the convolutional autoencoders learned for the MNIST and CelebA face dataset

Adversarial Networks for Quality Assessment

Layer (type)	Output Shape	Param #
input_1 (InputLayer)	(None, 128)	0
dense_1 (Dense)	(None, 256)	33024
dense_2 (Dense)	(None, 512)	131584
dense_3 (Dense)	(None, 256)	131328
dense_4 (Dense)	(None, 2)	514
Total params: 296,450		
Trainable params: 296,450		
Non-trainable params: 0		

MNIST Dataset

Layer (type)	Output Shape	Param #
input_1 (InputLayer)	(None, 256)	0
dense_1 (Dense)	(None, 512)	131584
dense_2 (Dense)	(None, 1024)	525312
dense_3 (Dense)	(None, 512)	524800
dense_4 (Dense)	(None, 2)	1026
Total params: 1,182,722		
Trainable params: 1,182,722		
Non-trainable params: 0		

CelebA Dataset

Layer (type)	Output Shape	Param #
input_1 (InputLayer)	(None, 2)	0
dense_1 (Dense)	(None, 8)	24
dense_2 (Dense)	(None, 16)	144
dense_3 (Dense)	(None, 8)	136
dense_4 (Dense)	(None, 2)	18
Total params: 322		
Trainable params: 322		
Non-trainable params: 0		

Ring-Square-Line Dataset

Figure 8. Details of the deep binary classifiers used for scoring the fitness of GMMs.



(a)



(b)

Figure 9. GMM Samples Generated from the GMM learned from EM-GMM (a), and from SW-GMM (b). Each column depicts random samples from a single component of the GMM.